



DOI: 10.29026/oea.2019.190010

Enhanced organic solar cell performance: Multiple surface plasmon resonance and incorporation of silver nanodisks into a grating-structure electrode

Thitirat Putnin^{1,2}, Chutiparn Lertvachirapaiboon¹, Ryousuke Ishikawa¹, Kazunari Shinbo¹, Keizo Kato¹, Sanong Ekgasit³, Kontad Ounnunkad^{2*} and Akira Baba^{1*}

In this study, plasmonic nanostructures were examined to enhance the light harvesting of organic thin-film solar cells (OSCs) by multiple surface plasmon resonance (SPR) phenomena originating from the grating-coupled configuration with a Blu-ray Disc recordable (BD-R)-imprinted aluminum (Al) grating structure and the incorporation of a series of silver nanodisks (Ag NDs). The devices with such a configuration maximize the light utilization inside OSCs via light absorption, light scattering, and trapping via multiple surface plasmon resonances. Different types and sizes of metallic nanoparticles (NPs), i.e., gold nanoparticles (Au NPs), Ag nanospheres (Ag NSs), and Ag NDs, were used, which were blended separately in a PEDOT:PSS hole transport layer (HTL). The device structure comprised of grating-imprinted-Al/P3HT:PCBM/Ag ND:PEDOT:PSS/ITO. Results obtained from the $J-V$ curves revealed that the power conversion efficiency (PCE) of grating-structured Al/P3HT:PCBM/PEDOT:PSS/ITO is 3.16%; this value is ~6% higher than that of a flat substrate. On the other hand, devices with flat Al and incorporated Au NPs, Ag NSs, or Ag NDs in the HTL exhibited PCEs ranging from 3.15% to 3.37%. Furthermore, OSCs with an Al grating substrate were developed by the incorporation of the Ag ND series into the PEDOT:PSS layer. Compared with that of a reference device, the PCEs of the devices increased to 3.32%–3.59% (11%–20% improvement), indicating that the light absorption enhancement at the active layer corresponds to the grating-coupled surface plasmon resonance and localized surface plasmon resonance excitations with strong near-field distributions penetrating into the active layer leading to higher efficiencies and subsequent better current generation.

Keywords: grating-coupled surface plasmon resonance; localized surface plasmon resonance; Ag nanodisks; organic solar cells; imprinted grating

Putnin T, Lertvachirapaiboon C, Ishikawa R, Shinbo K, Kato K *et al.* Enhanced organic solar cell performance: Multiple surface plasmon resonance and incorporation of silver nanodisks into a grating-structure electrode. *Opto-Electron Adv* 2, 190010 (2019).

Introduction

Organic solar cells (OSCs) with a bicontinuous interpenetrating network between a polymer donor and a fullerene acceptor exhibit potential advantages, including

lightweight nature, flexibility, feasible large-area devices, and cost-effective roll-to-roll fabrication¹⁻⁵. Despite the increase in the OSC efficiency to 11% and 13% for single- and tandem-junction structures, respectively⁶, its power conversion efficiency (PCE) is still less than those of their

¹Graduate School of Science and Technology, Niigata University, 8050 Ikarashi-2-nocho, Nishi-ku, Niigata 950-2181, Japan; ²Department of Chemistry and Center of Excellence for Innovation in Chemistry (PERCH-CIC), Faculty of Science and Center of Excellence in Materials Science and Technology, Chiang Mai University, Chiang Mai 50200, Thailand; ³Sensor Research Unit, Department of Chemistry, Faculty of Science, Chulalongkorn University, Bangkok 10330, Thailand.

*Correspondence: K Ounnunkad, E-mail: kontad.ounnunkad@cmu.ac.th; A Baba, E-mail: ababa@eng.niigata-u.ac.jp

Received: 28 March 2019; Accepted: 20 May 2019; Published: 14 July 2019

inorganic counterparts, with efficiencies approaching greater than 20%⁷. Typically, the PCEs of OSCs are limited because of the weak absorbance of the thin photoactive layer in the solar spectrum range. To solve this issue, the active layer thickness should be increased for a higher absorption of the incoming photons⁸. However, because the increase in the series resistance of the device leads to the limited charge carrier mobility of the polymers, leading to a limited active-layer thickness, it is still challenging to improve the light harvesting in OSCs. Hence, several techniques have been developed for, in turn, governing efficient optical absorption in films rather than improving the optical absorption depth. Thus, the surface structures of each OSC component, such as periodic patterns or rough surfaces, can increase the effective optical path of incident light inside absorbing materials via light trapping or scattering.

Recently, several light-trapping methods for OSCs were investigated following the development of wave optics and nanotechnology. By scattering light into the active layers comprising nanoparticles (NPs)^{9,10} or textured substrates^{11,12}, the considerable enhancement of light absorption has been reported¹³. The plasmonic effect for the enhanced optical absorption has been reported to occur via the excitation of localized surface plasmon resonance (LSPR) at metal NPs, propagation of the surface plasmon polariton modes, and the scattering enhancement^{14–16}.

In a majority of the imprinting processes, the nanoimprinting lithography technique (NIL) is one of the alternative methods due to its simplicity for transferring a pattern from a master mold to a substrate surface¹⁷. Moreover, the NIL technique has been reported to be a rapid imprinting process, affording large nanopatterned areas¹⁸. Typically, polydimethylsiloxane (PDMS) has been used as a patterning master mold in this technique¹⁹. The PDMS mold works with a complete conformal contact during the patterning of the substrate surface, even for the substrates with uneven surfaces. Compared to conventional photolithography, soft lithography using the elastomeric PDMS mold exhibits several advantages, particularly patterning of sensitive materials, such as polymers, cost-effectiveness, and the absence of an optical diffraction limit. It permits the control of the chemistry, patterning of large areas, and scalable production of patterned surfaces. Hence, to improve solar-cell performances, this NIL process has been recently employed for the formation of an irregular nanoscale-featured surface by using nanoporous anodic aluminum oxide (AAO) membrane filters²⁰, the formation of ordered nano/microstructures by using a large-scale nanoporous Si mold and AAO templates^{21,22}, and the formation of a grating structure by Blu-ray movie discs (BD) and Blu-ray disc-recordable (BD-R)^{23,24}. The latter involves the plasmonic effect at the patterned metallic electrodes. Recently, the nanoimprinting or grating-coupled process to fabricate a periodic 1-D grating structure at the electrode

has been demonstrated using BD-R to enhance the electric field in photoelectric conversion systems²⁴. The grating-coupled technique is a prism-less, convenient, propagating SPR excitation method^{25–27}. In the absence of SP excitation, light scattering and light trapping can occur on the grating-structured surface, improving the obtained photocurrent^{28,29}. Hence, the dramatic improvement in photovoltaic cell performance is expected as the SP field can be enhanced on the grating substrate, in addition to light scattering³.

Notably, by utilizing the LSPR effect of metallic nanoparticles (NPs) such as Au nanoparticles (Au NPs) and Ag nanoparticles (Ag NPs), NPs can be introduced into each part of the OSC devices for highly improved light harvesting^{30–36}. Although some studies have reported the improvement of %PCEs by the incorporation of different metallic NPs into OSCs^{37–40}, their effects on the charge separation and transport related to the high-efficiency of BHJ OSCs still need to be investigated in detail. Several research groups have reported that the presence of Ag NPs in the PEDOT:PSS HTL of OSCs leads to enhanced light harvesting performance due to their superior scattering efficiencies compared with those of other metallic NPs⁴¹. Moreover, the incorporation of silver nanodisks (Ag NDs) in OSCs has been rarely reported. Ag NDs, which are a type of Ag nanoprisms, have attracted considerable attention due to their extreme degrees of anisotropy, morphologically dependent plasmonic properties, and a wide range of light absorption and light scattering from visible to near-infrared region^{42–44}. The incorporation of Ag NDs is expected to improve the light absorption, light scattering, and light trapping in OSCs. Hence, Ag NDs are selected herein.

Both synergistically performing plasmonic effects, namely localized plasmon and propagating grating-coupled SP, are of interest in developing new generation of plasmonic photovoltaic cells²⁷. The improvement of light trapping and management of light harvesting in OSCs can be rendered by plasmonic effects, such as LSPRs from two metallic NPs (i.e., Ag NPs + Au NPs, respectively)⁸ or LSPRs from two shapes (i.e., Au nanorods + Au nanospheres, respectively)⁴⁵ and the LSPR–GCSPR effect from Au NPs + Ag NPs + 1-D grating-structured Al electrode⁴⁶. The excitation of free electrons in metal NPs or at metal/dielectric interfaces leads to the storage and enhancement of energy in the LSPR at the NPs or in the propagating SPs at the metal/dielectric interfaces, which can be converted into absorption events in the active layers via a near-field effect or far-field coupling^{47–50}.

In this study, OSCs based on the imprinted 1-D grating structures were designed and fabricated on an active layer of an organic thin film as the support for an Al electrode, and the Ag ND series were incorporated into the HTL of a BHJ solar cell for improving the light trapping via the multiple plasmonic effects of the grating-structured Al

and metal NPs. The cooperative multiple plasmonic effect exhibits advantages, including broader light absorption enhancement, enhanced exciton generation rate and dissociation efficiency, and increased charge carrier density and lifetime. Moreover, finite-difference time-domain (FDTD) simulations were performed to investigate the electric-field distribution around the surfaces of the Ag ND series and metallic grating, confirming the multiple plasmonic effect.

Experimental details

Synthesis of Ag nanodisks

Ag NSs and Ag NDs were synthesized according to the previously reported studies^{44,51}. First, Ag NSs were synthesized by chemical reduction using NaBH_4 (Merck) as the reductant. The diameters of the Ag NSs ranged from 6 to 7 nm. The Ag NDs were synthesized by the chemical-shape transformation of Ag NSs. Briefly, 2.272 mL of a 30% w/w H_2O_2 (Merck) solution was injected into 200 mL of a Ag NS colloid by using a syringe pump at a rate of $13.45 \text{ mL}\cdot\text{min}^{-1}$ under vigorous stirring. As the H_2O_2 :Ag NS molar ratio is the key parameter for controlling the LSPR wavelengths of the Ag NDs used herein, it was varied from 0 to 15. After the addition of the H_2O_2 solution, the colloid solution was further stirred for another 10 min to ensure a complete reaction, and the average diameters of Ag NDs ranged from 30 to 70 nm.

Preparation of the PDMS grating mold

The grating structure was duplicated from the BD-R master template. To obtain BD-R master templates, BD-Rs were first cut into small rectangles before removing the dye coating using concentrated HNO_3 for 20 min. Second, the BD-R grating substrate was subsequently cleaned using detergent, distilled water, and deionized water by ultrasonication for 20 min in each step, followed by drying the substrate by N_2 gas. Liquid PDMS was prepared by the mixing of a silicone elastomer base and a silicone elastomer curing agent in a ratio of 10:1 (13 g) in a plastic glass under stirring. The liquid PDMS was poured on the master template, and the air bubble in the PDMS was removed at 70°C in a vacuum oven for 3 h. After cooling to room temperature, the master template was detached from the PDMS duplicate.

Preparation of solar cell devices

Indium-doped tin oxide (ITO) glass substrates (Furuuchi Chemical Co., Ltd., $10 \Omega/\text{cm}^2$) were cleaned using a detergent, distilled water, and deionized water by ultrasonication for 20 min for each step, followed by drying under N_2 gas. After drying, the substrates were exposed to ultraviolet ozone plasma for 20 min. The hole-transporting material (HTM) PEDOT:PSS solution (Clevios, Heraeus Co.) was blended with 20% v/v of metallic NPs. The mixture solution was spin-coated on the ITO substrate at 1000 rpm for 90 s, and the resultant sub-

strate was dried at 120°C in a vacuum oven for 10 min. Poly (3-hexylthiophene) (P3HT) (Sigma-Aldrich) and phenyl C61-butyric acid methyl ester (PC_{61}BM) (Sigma-Aldrich) were mixed in a weight ratio of 1:0.8 in 1.0 mL of 1, 2-dichlorobenzene (Kanto Chemical Co. Inc.,) for 24 h. The photoactive layer was spin-coated at 1000 rpm for 15 s and 1500 rpm for 45 s, respectively, and imprinted with the grating-pattern PDMS mold by thermal imprinting at 100°C in a vacuum oven for 60 min. Then, aluminum film (150 nm) was deposited by vacuum evaporation. Finally, the device was annealed at 150°C for 45 min in a vacuum oven. The active areas of these devices were 1.0 cm^2 . The devices based on Au NPs (Sigma-Aldrich) and Ag NDs with different diameters, including 30, 40, 50 and 70 nm incorporated into the PEDOT:PSS layer, were prepared using a similar process. Figure 1 shows the schematic of the fabricated OSC devices. In addition, reference cells were prepared with the same configuration without NPs and grating.

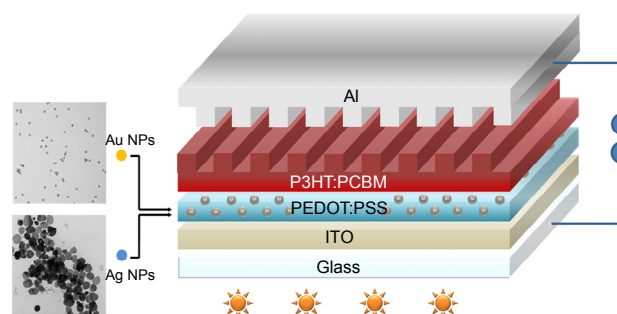


Fig. 1 | Schematic of organic solar cell devices.

Characterization

The optical properties of the as-prepared materials and devices were investigated using a UV-visible spectrophotometer (V-650, Jasco). The morphology of the Ag ND series was observed by transmission electron microscopy (TEM, JEOL Ltd., USA). The surface morphology of the prepared films was analyzed by atomic force microscopy (AFM, SPM-9600, Shimadzu). Under an ambient environment, current density-voltage (J - V) curves and impedance spectra of all the fabricated OSCs were recorded under irradiation by using a solar simulator (HAL-C100, 100-W compact xenon light source, Asahi Spectra) equipped with a precision source-meter unit (B2901A, Agilent) and a potentiostat (PARSTAT 4000, Princeton Applied Research), respectively. The solar cell was operated under illumination with a light intensity of 75 mW cm^{-2} . Incident photon-to-current efficiency (IPCE) properties were measured using a Merlin monochromator with a 300-W xenon as the light source.

Results and discussion

To examine the effect of incorporating plasmonic nanostructures into the solar cell devices, the active layer was imprinted using a grating structure, and the HTL was

incorporated with metallic NPs. In addition, the optimization of the active-layer film thickness, NP content, and type of NPs was examined. In our experiment, the following cells were designed; (1) reference device: Al/P3HT:PCBM/PEDOT:PSS/ITO, (2) device with the grating structure: grating-patterned Al/P3HT:PCBM/PEDOT:PSS/ITO, (3) device with metallic NPs: Al/P3HT:PCBM/Au NP, Ag NS, or Ag ND series-PEDOT:PSS/ITO, (4) device with the grating structure and metallic NPs: grating-patterned Al/P3HT:PCBM/(Au NP, Ag NS or Ag ND series-PEDOT:PSS/ITO.

Optical properties and surface morphology

To investigate the particle shapes and sizes of metallic NPs, TEM images of monodisperse Au NPs and the Ag NS and Ag ND series were recorded (Fig. S1). Au NPs were highly dispersed with an average diameter of 5 nm. In the case of the Ag ND series, after the injection of H_2O_2 into the Ag NS solution, the solution color instantaneously changed from yellow to red, pink, violet, or blue depending on the molar ratio between H_2O_2 and the Ag NSs. TEM images revealed the good dispersion of the Ag ND series in deionized water, with average diameters ranging from 30 to 70 nm, denoted as Ag NDs-30, Ag NDs-40, Ag NDs-50, and Ag NDs-70, respectively. Figure 2 shows the UV-vis-NIR absorption spectra of Au NP, Ag NS, or Ag ND series solutions: Plasmon resonance peaks

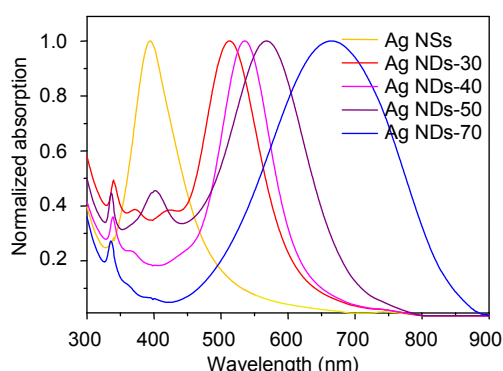


Fig. 2 | UV-visible absorption spectra of Ag NSs and AgNDs in solutions.

corresponding to Ag NSs, Ag NDs-30, Ag NDs-40, Ag NDs-50, and Ag NDs-70 in the solution phase were observed at 410, 510, 535, 570, and 660 nm, respectively. The color and spectral changes were directly related to the morphological transformation of the Ag NPs.

Figure S2 shows the AFM images of PEDOT:PSS HTLs with and without the metallic NPs. The root-mean-square (RMS) roughness (R_a) of the PEDOT:PSS layer on ITO glass was calculated to be 1.7 nm (Fig. S2(a)), while those of PEDOT:PSS blended with Au NPs, Ag NSs, Ag NDs-30, Ag NDs-40, Ag NDs-50, or Ag NDs-70 were 1.8, 2.4, 2.2, 2.3, 2.4, or 2.4 nm, respectively (Figs. S2(b–g)). This result indicated that all the metallic NPs slightly increase the R_a of PEDOT:PSS HTL. Figure S3 shows the morphology of the active layer after imprinting with the 1-D grating. The R_a of the active layer on PEDOT:PSS-coated ITO glass was calculated to be 2.4 nm (Fig. S3(a)) while that of the active layer after imprinting with the 1-D grating was calculated to be 4.9 nm (Fig. S3(b)). Moreover, the R_a values for the photoactive layer imprinted with the 1-D grating on PEDOT:PSS HTLs containing Au NPs, Ag NSs, Ag NDs-30, Ag NDs-40, Ag NDs-50, or Ag NDs-70 were 3.2, 4.8, 4.6, 4.3, 4.1, or 3.6 nm, respectively (Fig. S3(c–h)). Notably, the active layer imprinted with the 1-D grating with the metallic NPs exhibited no clear increase in the R_a value compared to the 1-D grating active layer without the metallic NPs.

Photovoltaic performance of solar cells

To investigate the effect of different metallic NPs in OSCs, two solar-cell systems based on PEDOT:PSS films containing Au NPs or Ag NDs-30 with similar resonance plasmonic peaks (i.e., 510 and 520 nm) were prepared, and their multiple plasmonic effect, including metallic NPs in the HTL and Al cathode with a grating structure, was examined. Figure 3 shows the $J-V$ curves for the control device, device with the Al grating cathode, device with the Au NPs-incorporated HTL, device with Ag NDs-30-incorporated HTL, device with Au NPs- blended HTL on the grating-structured Al cathode, and the device with Ag NDs-30-mixed HTL on the grating-structured Al

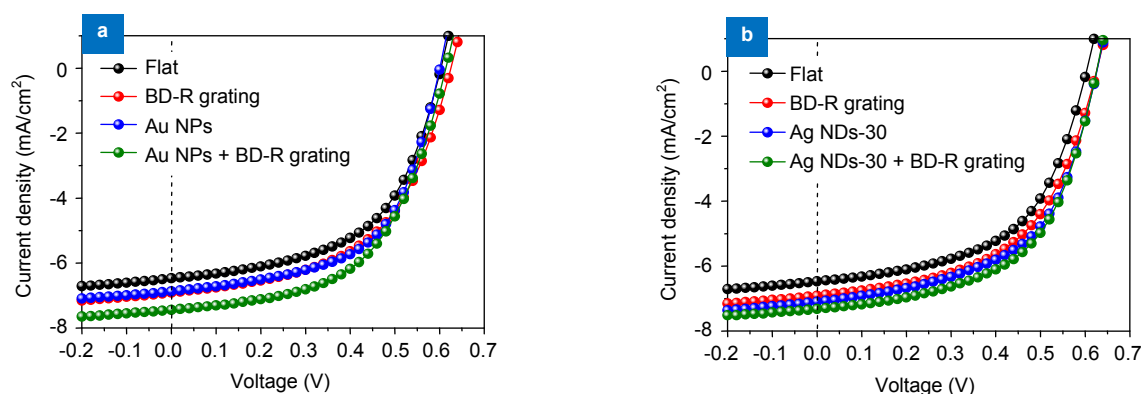


Fig. 3 | $J-V$ curves of the device systems. (a) Au NPs and (b) Ag NDs-30 incorporated into the PEDOT:PSS layer.

Table 1 | Photovoltaic performances of OSCs devices from Figure 3.

Devices	J_{sc} (mA/cm ²)	V_{oc} (V)	FF	PCE (%)	Improvement (%)
Control	6.42	0.60	0.58	2.98	
Grating	6.99	0.61	0.55	3.16	6.04
Au NPs	6.87	0.60	0.57	3.15	5.70
Au NPs + grating	7.44	0.61	0.55	3.36	12.75
Ag NDs-30	7.01	0.63	0.55	3.27	9.73
Ag NDs-30 + grating	7.32	0.63	0.56	3.42	14.76

cathode. Table 1 summarizes the photovoltaic performances of such solar cell devices. The incorporation of Au NPs in HTL led to the increase in the short-circuit current densities (J_{sc}) of the device from 6.42 to 6.87 mA/cm², while significant changes in the open-circuit voltage (V_{oc}) and FF were not observed. Hence, PCE is enhanced from 2.98% to 3.15%. In the same manner, the incorporation of Ag NDs-30 into the HTL exhibited improved device performance. Enhanced J_{sc} and V_{oc} values of 7.10 mA/cm² and 0.63 V, respectively, were observed. Improved FF and PCE values of 0.55 and 3.27%, respectively, were observed, indicating that the presence of Au NPs or Ag NDs-30 in the PEDOT:PSS HTL leads to the enhancement of the solar-cell performance by the LSPR effect^{33,34}. To investigate the effect of the grating structure on light harvesting, the patterning Al cathode of OSCs was demonstrated. The grating structure on the OSC active layer completed by Al deposition also led to the improved OSC performance (Fig. 3(b)). With the grating structure, the PCE value increased to 3.16%, which would involve light scattering by the grating structure, leading to the increment of the light traveling path inside the active layer and subsequent increase in the light absorption by the active layer. Furthermore, the strong electric field originating from the GCSPR of the metallic grating enhanced the generated photocurrent, leading to the increase in the J_{sc} and PCE values²³. As previously studied, 1-D grating structure exhibits the light polarization dependence for the excitation of propagating-surface plasmon in the OSCs⁵². Moreover, the multiple plasmonic effect, including the metallic NPs in the HTL and grating architecture of the Al cathode, was examined: The solar cell based on the Au NP-incorporated HTL and the imprinted Al cathode exhibited better performance than that of the device with the Al grating without Au NPs. The device with a multiple plasmonic system based on Au NPs exhibited an increased J_{sc} value of 7.44 mA/cm², with significant changes in the V_{oc} and FF values and a resultant enhanced %PCE of 3.36. Similarly, the device based on Ag NDs-30 in the HTL and grating-imprinted Al electrode exhibited better performance than the imprinted device without Ag NDs-30. Enhanced performance, i.e., a J_{sc} of 7.32 mA/cm², a V_{oc} of 0.63 V, an FF of 0.56, and a PCE of 3.42%, was observed for this device. Hence, the devices imprinted with grating and incorporated with metallic NPs exhibit performance via the light scattering effect

and LSPR of the metallic NPs and GCSPR of the grating-structured Al cathode^{24,33–34}. Moreover, the imprinted device with the Ag NDs-30 incorporated into the HTL exhibited the best performance, corresponding to the higher light scattering of Ag NDs-30⁵³. In this study, the light-harvesting management using the Ag ND series together with the metallic grating is interesting to achieve the broadband plasmonic absorption as well as the highest device performance.

To examine the effect of the Ag ND series and its multiple plasmonic configuration on the light-harvesting ability, the photocurrents of OSCs were measured. Figures 4(a) and 4(b) show the corresponding $J-V$ curves of the devices with and without the incorporation of the Ag ND series, grating-structured Al cathode, and the multiple plasmonic system in comparison with that of the control device. Furthermore, Figs. S4(a) and S4(b) show the corresponding IPCE properties. Table 2 summarizes the performances and properties of such solar cells. Few studies have reported the use of Ag NPs together with patterned Al for constructing OSCs. In this study, the improvement of light harvesting by the incorporation of the Ag NS and Ag ND series, including Ag NDs-30, Ag NDs-40, Ag NDs-50, and Ag NDs-70, into the HTL (Fig. 4(a)), as well as with grating-structured Al, was first investigated (Fig. 4(b)). After the incorporation of the Ag NS or Ag ND series into the PEDOT:PSS layer, J_{sc} increased by 7% to 10%, while FF remained nearly constant, and the PCE slightly increased with the Ag NP diameter. For devices constructed using Ag NSs, Ag NDs-30, Ag NDs-40, Ag NDs-50, and Ag NDs-70, their PCE values increased from 2.98% to 3.22%, 3.27%, 3.29%, 3.33%, and 3.37%, respectively, compared with that of a control device fabricated under similar conditions.

After the incorporation of the Ag NS and Ag ND series into the PEDOT:PSS layer, the improved OSC performance might result from the following possible factors. First, the optical path length of the active layer can be increased because of the trapped light via multiple high-angle scattering from the Ag NS and Ag ND series. According to the well-known Mie theory⁵⁴, the total Mie extinction is a sum of the contributions from the absorption and scattering components, and large particles exhibit a large scattering cross section. The sizes of the Ag NS and Ag ND series ranged from 6 to 70 nm. Moreover, the density of Ag NS and Ag ND series is relatively low

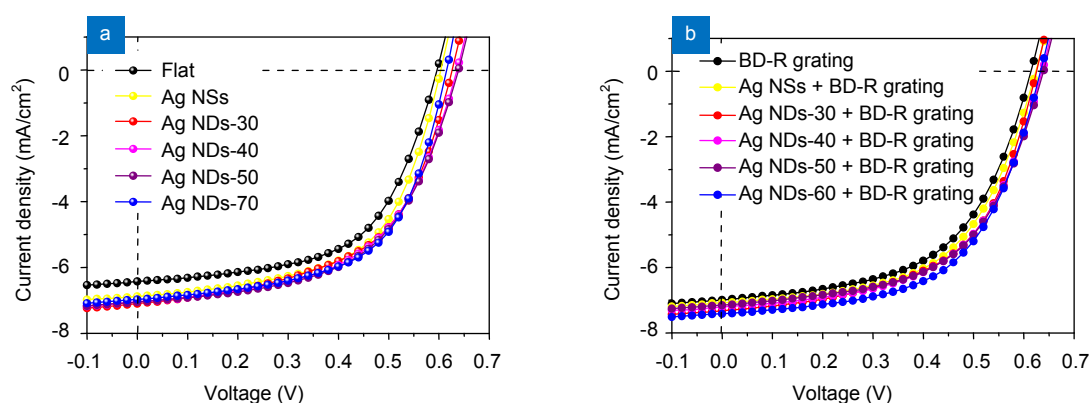


Fig. 4 | J - V curves of the devices incorporated with (a) different Ag NDs in the PEDOT:PSS layer and (b) different Ag NDs in the PEDOT:PSS layer and grating-imprinted Al electrode.

Table 2 | Photovoltaic performances of OSCs devices from Figure 4.

Devices	LSPR peak wavelength (nm)	Grating	J_{sc} (mA/cm ²)	V_{oc} (V)	FF	PCE (%)	Improvement (%)
Control	-	-	6.42	0.60	0.58	2.98	-
Grating	-	+	6.99	0.61	0.55	3.16	6.04
Ag NSs	410	-	6.88	0.60	0.58	3.22	8.05
Ag NSs	410	+	7.08	0.62	0.56	3.32	11.41
Ag NDs-30	510	-	7.10	0.63	0.55	3.27	9.73
Ag NDs-30	510	+	7.32	0.63	0.56	3.42	14.76
Ag NDs-40	535	-	7.05	0.64	0.55	3.29	10.40
Ag NDs-40	535	+	7.21	0.64	0.56	3.42	14.76
Ag NDs-50	570	-	7.05	0.64	0.56	3.33	11.74
Ag NDs-50	570	+	7.15	0.64	0.56	3.43	15.10
Ag NDs-70	660	-	6.97	0.62	0.59	3.37	13.09
Ag NDs-70	660	+	7.41	0.63	0.57	3.59	20.47

and optimized. Hence, the device performance was not decreased by the light absorption loss. The efficiency increases in the wide wavelength range shown in Fig. S4(a) indicates the light scattering effect in the OSCs. Second, the LSPR of the Ag NS and Ag ND series can produce large local electromagnetic fields near the nanoparticle surface, and the resulting local-field enhancement increases the light absorption of organic materials, improving the overall device efficiency. With the increase in the particle size, the decay distance of the local field increased, and the light scattering of OSCs was enhanced. Hence, the near field extends into the active layer to a large extent, and the possibility of the interaction coupling between the near field and incident light in the active layer increases, enhancing the photogeneration of excitons in the active layer. Hence, the PCEs of plasmonic solar cells increase with the Ag ND particle size. In addition, the wavelength range for the spectral response enhancement was consistent with the plasmon resonance peak of the Ag NS and Ag ND series, indicating that the LSPR excitation is responsible for the PCE enhancement.

Notably, the combination of both plasmonic nanostructures, viz. Ag NP/Au NPs and metallic grating, respectively, into photoelectric conversion systems af-

forded excellent preliminary results²⁷, suggesting that solar cells harvest solar light with the synergistic effect of such plasmonics. To improve their performances, the multiple plasmonic effect originating from the Ag ND series and the grating-coupled Al cathode was achieved herein. The imprinted Al-grating-based OSCs with HTLs containing Ag NSs, Ag NDs-30, Ag NDs-40, Ag NDs-50, and Ag NDs-70 exhibited increased J_{sc} values of 10% to 15%, with enhanced PCE values ranging from 2.98% to 3.32%, 3.42%, 3.42%, 3.43% and 3.59%, respectively. This result indicated that the light absorption enhancement at the active layer is related to the LSPR excitation with strong near-field distributions penetrating into the absorption polymer and GCSPP from the metallic grating, leading to higher efficiencies due to the increased absorption and subsequent better current generation.

SPR reflectivity properties

To investigate the propagating SPR excitation on the Al grating, the reflectivity of the OSCs on the irradiation of white light from the ITO glass side was measured as a function of the wavelength at fixed incidence angles from 20° to 70° (Fig. 5). Figures 5(a) and 5(c) show the reflectivity curves of the devices without a grating (flat Al) and

with/without the incorporation of the Ag NDs into the HTL in the wavelength region of 400–800 nm. At wavelengths of greater than 500 nm, with p-polarized light, the dip peak at the resonant wavelength was not observed (Figs. 5(a) and 5(c)). On the other hand, Figs. 5(b) and 5(d) show the SPR reflectivity dips for the devices with only the Al grating and combination of the Al grating and incorporation of Ag NDs. In the figures, the reflectivity decrease caused at the localized plasmon wavelength of Ag NDs was not observed due to the low density of incorporated Ag NDs. The dip peak in each reflection spectrum corresponding to the surface plasmon excitation was observed at 650–750 nm under p-polarized light irradiation. With the increase in the incidence angle, the dip peak exhibited a red-shift from 650 nm to 750 nm, confirming the SPR properties of the fabricated Al grating on the top devices. Although studies have not reported the SPR reflectivity curve at an incidence angle of 0° due to the limited experimental configuration, the SPR dip wavelength at 0° is expected to be located at 580–650 nm from the trend of the SPR dip wavelength dependence, revealing that grating-coupled SPR can enhance the generation of photocarriers in the active layer of OSCs as the photovoltaic properties are measured under light irradiation at 0° . This result revealed that the improved J_{sc} of the devices with the 1-D grating is related to the improved light absorption due to light scattering and GCS-SPR.

Impedance spectroscopy

Figure 6 shows the impedance spectra recorded under illumination for examining the resistance and charge transfer of the proposed devices: Semicircles were observed in the Nyquist plots. Table 3 summarizes the %PCE, J_{sc} , R_s , and R_{ct} values for OSCs. Impedance spectra typically exhibited a large semicircle in the low-frequency region. Moreover, the values for the real part (Z') and the imaginary part (Z'') of the complex impedance noticeably decreased, in addition to the increase in the absorption wavelength of the Ag ND series, leading to the decrease in the semicircle diameter of the charge-transfer resistance. The semicircle diameter for the solar-cell devices without the Ag ND series was considerably greater than those of devices with the Ag ND series, and the semicircle diameter slightly decreased with the increase in the average Ag ND diameter (Fig. 6(a)). Moreover, the semicircle diameters for the devices incorporated with different Ag NDs were considerably greater than those of the devices with the incorporated Ag NDs and imprinted Al-grating electrode (Fig. 6(b)), indicative of the lowest charge-transfer resistance for multiple plasmonic devices. Notably, the decrease in the equivalent resistance by the introduction of the Ag ND series in the PEDOT:PSS layer and Al grating led to the effective decrease in the series resistance of the devices, which is consistent with the enhanced photocurrent. Figures 6(a) and

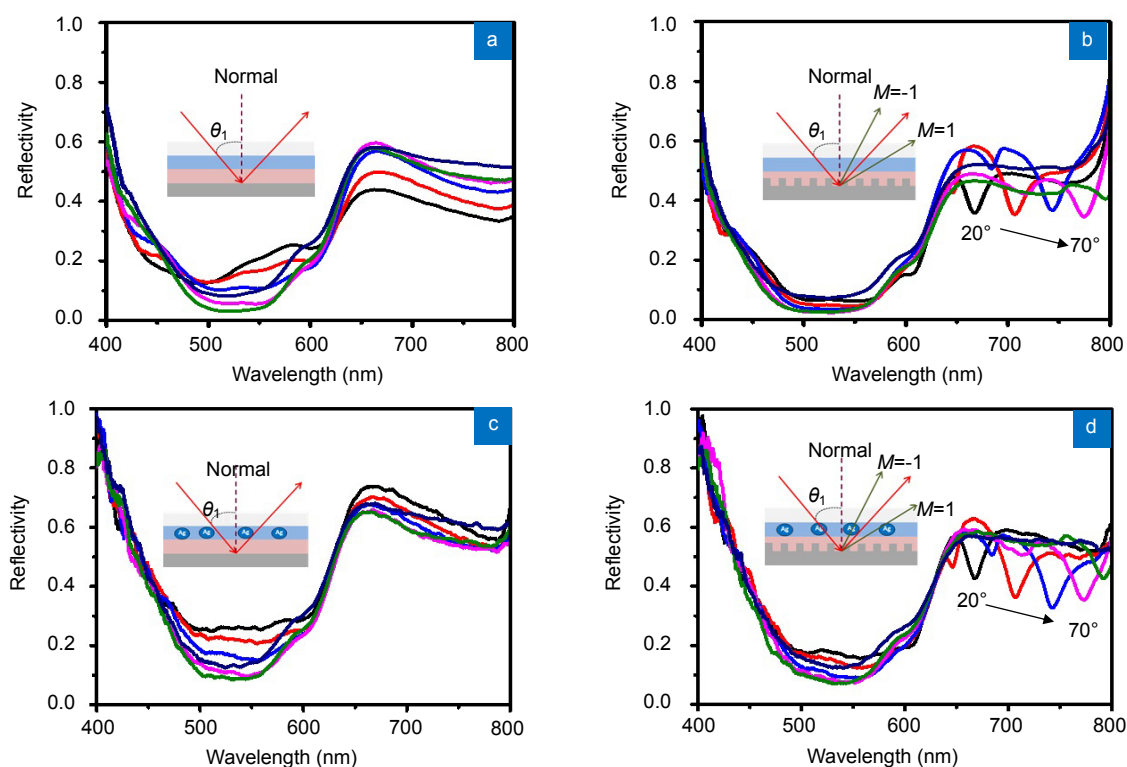


Fig. 5 | SPR reflectivity curves of the solar cells with p-polarization at various incidence angles from 20° to 70° for a (a) flat Al electrode, (b) grating Al electrode, (c) PEDOT:PSS incorporated with Ag NDs, and (d) PEDOT:PSS incorporated with Ag NDs and the grating Al electrode.

6(b) show the equivalent circuit of these OSCs, and Table 3 summarizes the series resistance (R_s) and charge-transfer resistance (R_{ct}) values. The R_s value of the device with the Al grating decreased from 10.12 Ω to 9.37 Ω while the incorporation of the Ag ND series into the HTL further decreased the R_s value. With the increase in the particle size of Ag NDs, the R_s value additionally decreased. The lowest R_s value was observed for the device with the imprinted Al-grating electrode and incorporated with the Ag ND series. Similarly, the device with the Al grating exhibited an R_{ct} value less than that of the control device. With the increase in the Ag ND particle size, the devices incorporated with the Ag ND series exhibited a

slightly decreased R_{ct} value. The device with the Al grating and incorporated with the Ag ND series exhibited an R_{ct} value less than those of the devices with only the Al grating or only incorporation of the Ag ND series into the HTL, indicating that the Al grating structure and/or Ag ND series can improve the interfacial contact and charge-transfer properties of OSCs. Figures 6(c) and 6(d) show the maximum frequency peaks of the Bode phase plots for OSCs.

Compared to the control device, the device with only the Al grating exhibited a higher frequency peak. The devices incorporated with only the Ag ND series exhibited frequency peaks that were slightly shifted to higher

Table 3 | Power conversion efficiency (PCE), short-circuit current density (J_{sc}), average electron lifetime (τ_{avg}), maximum frequency (f_{max}), contact resistance (R_s), and charge-transfer resistance (R_{ct}) of fabricated OSCs.

Devices	PCE (%)	J_{sc} (mA/cm ²)	τ_{avg}	f_{max}	R_s	R_{ct}
Control	2.98	6.42	4.80	33.17	10.12	10.13
Grating	3.16	6.99	5.00	31.85	9.37	8.69
Ag NSs	3.22	6.88	4.60	34.62	8.45	10.77
Ag NSs + grating	3.32	7.08	4.60	34.62	8.45	7.73
Ag NDs-30	3.27	7.10	4.60	34.62	8.34	10.66
Ag NDs-30 + grating	3.42	7.32	4.80	33.17	8.34	7.65
Ag NDs-40	3.29	7.05	4.80	33.17	8.23	10.64
Ag NDs-40 + grating	3.42	7.21	4.60	34.62	8.23	7.63
Ag NDs-50	3.33	7.05	4.80	33.17	8.22	10.35
Ag NDs-50 + grating	3.43	7.15	4.80	33.17	8.22	7.30
Ag NDs-70	3.37	6.97	4.80	33.17	8.13	10.20
Ag NDs-70 + grating	3.59	7.41	5.00	31.85	8.13	6.80

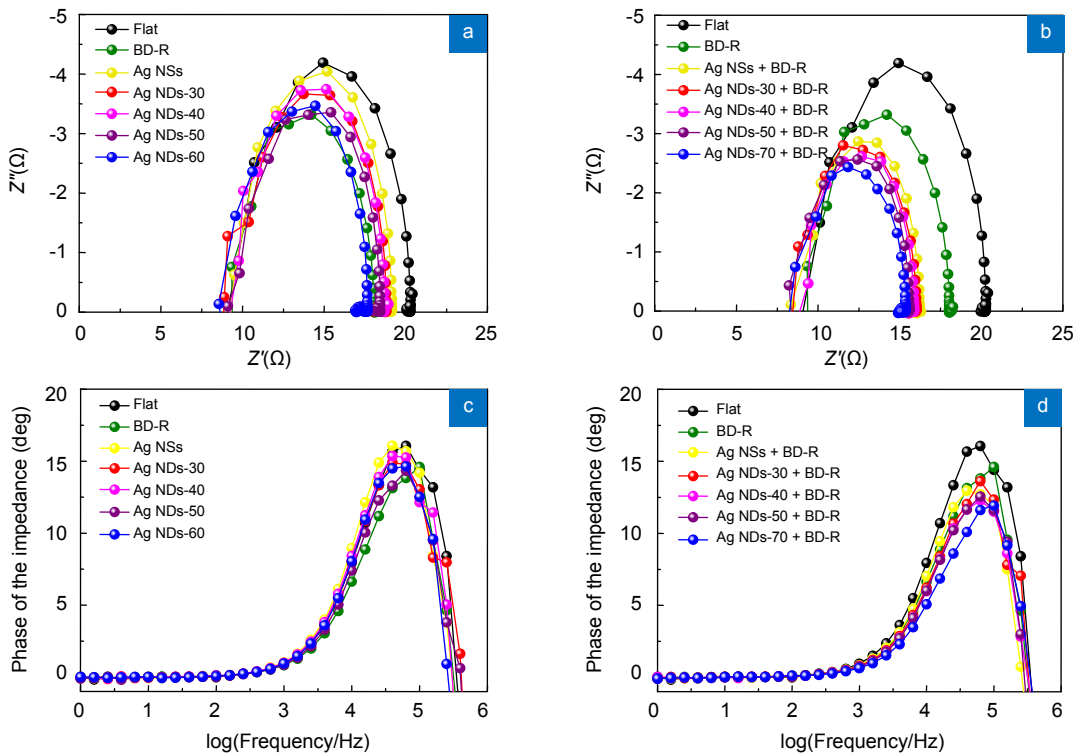


Fig. 6 | Nyquist plots of the devices: (a) incorporated with Ag NDs with different LSPR peaks and (b) incorporated with Ag NDs with different LSPR peaks and imprinted Al grating. Bode phase plots: (c) corresponding to (a), and (d) corresponding to (b).

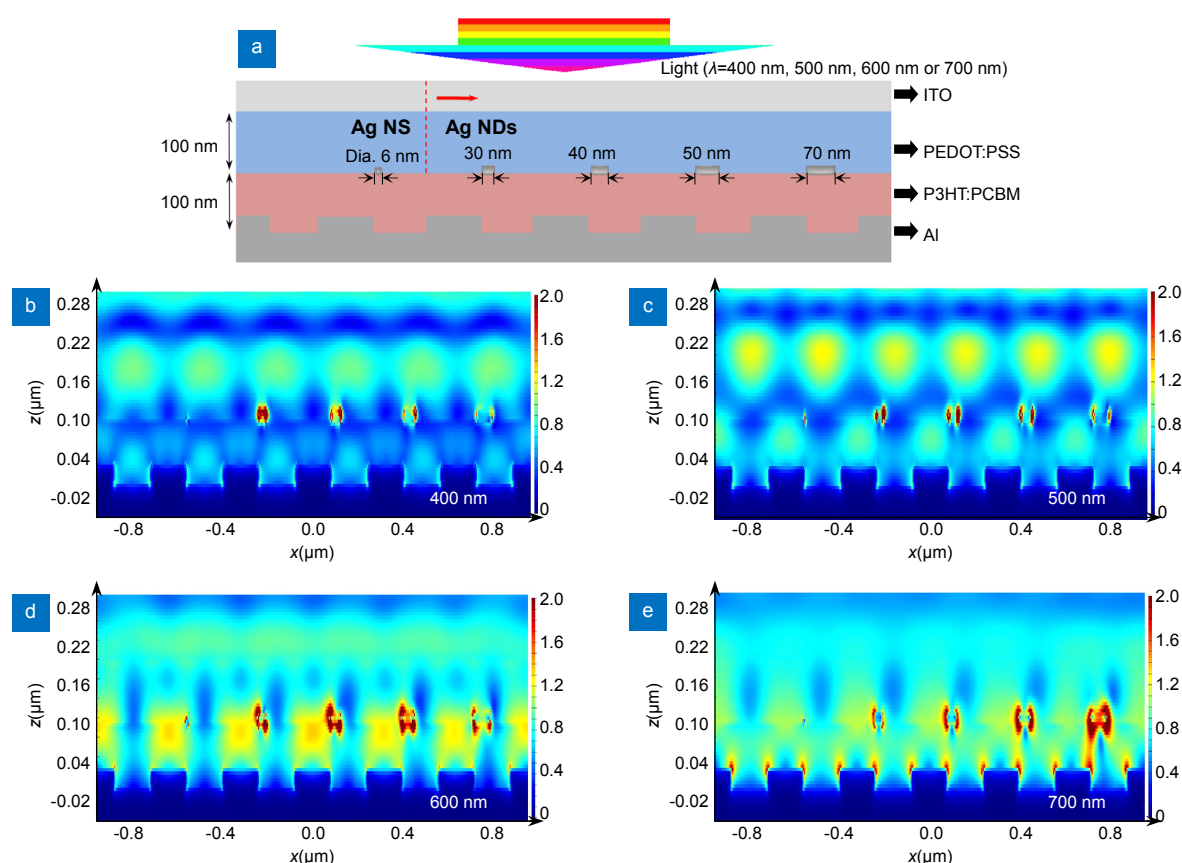


Fig. 7 | Schematic of the simulated structures (a) and electric-field intensity maps of OSCs with Ag NSs (diameter of 6 nm) and Ag NDs (diameter of 30, 40, 50, and 70 nm and a thickness of 15 nm) in the PEDOT:PSS layer at illumination wavelengths of (b) 400 nm, (c) 500 nm, (d) 600 nm, and (e) 700 nm.

frequencies with the increase in the particle size of the Ag NDs. In the same manner, the frequency peaks corresponding to the device with the Al grating and the incorporated Ag ND series slightly shifted with the increase in the Ag ND particle size. In addition, the electron or carrier lifetime (τ_{avg}), which is defined as the average time taken by an excess minority carrier to recombine⁵⁵, can be calculated from the Bode phase plots. Table 3 summarizes the τ_{avg} values. The average carrier lifetimes were not significantly different, suggesting that the Al-grating structure and Ag NDs in the HTL might not significantly affect the carrier lifetime. Hence, the performances of the designed devices with the grating-coupled configuration and the incorporation of the Ag ND series into the HTL are considered to be mainly improved by GCSRP, LSPR, and light scattering effect.

FDTD simulation

Furthermore, the FDTD simulation was employed to investigate the enhanced electric fields of the Ag NS and Ag ND series incorporated into the PEDOT:PSS layer by the Al-coated grating electrode (Fig. 7). Figure 7(a) shows the model device structure for the FDTD simulation. The device comprised Ag NSs with different sizes and the Al grating cathode. At a wavelength of 400 nm, the result

obtained from FDTD simulations clearly revealed that compared to the other Ag NDs, Ag NDs-30 exhibits a higher electric field enhancement, corresponding to the LSPR absorption spectra shown in Fig. 7(b). In the case of the incident light at a wavelength of 500 nm (Fig. 7(c)), the electric-field intensities at Ag NDs-30 and Ag NDs-40 were enhanced, while at 600 nm (Fig. 7(d)), the electric-field intensities of Ag NDs-40 and Ag NDs-50 were strongly enhanced, indicative of the good interface of the active layer/Al-coated grating surface. Moreover, at a wavelength of 700 nm (Fig. 7(e)), compared to the other sizes, Ag NDs-70 exhibited the highest electric-field intensity, and the electric field intensity of the active layer/Al interface exhibited strong enhancement. This result is related to the induction of the electric field surrounding both components. Hence, large Ag NDs can enhance the electric-field intensity, leading to the increased absorption, scattering, and trapping in the OSCs, affording high light-harvesting performance. Furthermore, the active layer/grating-structured Al interface enhanced the electric-field intensity in the range of 600–700 nm due to the GCSRP excitation, which can lead to coupling with the electric-field intensity of Ag NDs-50 and Ag NDs-70. This coupling in turn can lead to the higher photocurrent compared to the other sizes. This result confirmed the

synergistic effect of the GCSPP and LSPR simultaneous excitation. The FDTD simulation results showed good agreement with the results obtained from the J - V curves and IPCE.

Conclusions

In this study, enhanced OSC performance by exploiting multiple SPR phenomena originating from the grating-coupled technique and the incorporation of a series of plasmonic Ag NDs was successfully achieved. The imprinting of the grating structure on the P3HT:PCBM active layer completed by the Al electrode and/or the incorporation of Ag NDs into the HTL of the PEDOT:PSS, improved the light harvesting and power efficiency/device performances via the induced local-field enhancement. The developed plasmonic systems exhibited better absorption property, better light trapping and light scattering within the devices. The best OSC with the configuration of Al grating/P3HT:PCBM/PEDOT:PSS-Ag NDs-70/ITO exhibited improved %PCE of 20.47%. Moreover, cooperative plasmonic enhancement in OSCs by the combination of the grating structure and metal NPs would be exploited for the further development of other enhanced photovoltaics.

References

- Chen C C, Dou L, Zhu R, Chung C H, Song T B *et al.* Visibly transparent polymer solar cells produced by solution processing. *ACS Nano* **6**, 7185–7190 (2012).
- Ou Q D, Li Y Q, Tang J X. Light manipulation in organic photovoltaics. *Adv Sci* **3**, 1600123 (2016).
- Atwater H A, Polman A. Plasmonics for improved photovoltaic devices. *Nat Mater* **9**, 205–213 (2010).
- Chen J D, Cui C H, Li Y Q, Zhou L, Ou Q D *et al.* Single-junction polymer solar cells exceeding 10% power conversion efficiency. *Adv Mater* **27**, 1035–1041 (2015).
- Yang Y, Mielczarek K, Aryal M, Zakhidov A, Hu W. Nanoimprinted polymer solar cell. *ACS Nano* **6**, 2877–2892 (2012).
- You J B, Dou L T, Yoshimura K, Kato T, Ohya K *et al.* A polymer tandem solar cell with 10.6% power conversion efficiency. *Nat Commun* **4**, 1446 (2013).
- Bagher A M. Introduction to organic solar cells. *Sustain Energy* **2**, 85–90 (2014).
- Vohra V, Kawashima K, Kakara T, Koganezawa T, Osaka I *et al.* Efficient inverted polymer solar cells employing favourable molecular orientation. *Nat Photonics* **9**, 403–408 (2015).
- Lu L Y, Luo Z Q, Xu T, Yu L P. Cooperative plasmonic effect of Ag and Au nanoparticles on enhancing performance of polymer solar cells. *Nano Lett* **13**, 59–64 (2013).
- Yao M N, Shen P, Liu Y, Chen B Y, Guo W B *et al.* Performance improvement of polymer solar cells by surface-energy-induced dual Plasmon resonance. *ACS Appl Mater Interfaces* **8**, 6183–6189 (2016).
- Cai J G, Qi L M. Recent advances in antireflective surfaces based on nanostructure arrays. *Mater Horiz* **2**, 37–53 (2015).
- Munday J N, Atwater H A. Large integrated absorption enhancement in plasmonic solar cells by combining metallic gratings and antireflection coatings. *Nano Lett* **11**, 2195–2201 (2011).
- Chen B C, Cheng Y S, Gau C, Lee Y C. Enhanced performance of polymer solar cells with imprinted nanostructures on the active layer. *Thin Solid Films* **564**, 384–389 (2014).
- Sha W E I, Li X H, Choy W C H. Breaking the space charge limit in organic solar cells by a novel plasmonic-electrical concept. *Sci Rep* **4**, 6236 (2014).
- Choy W C H, Chan W K, Yuan Y P. Recent advances in transition metal complexes and light-management engineering in organic optoelectronic devices. *Adv Mater* **26**, 5368–5399 (2014).
- Baba A, Aoki N, Shinbo K, Kato K, Kaneko F. Grating-coupled surface Plasmon enhanced short-circuit current in organic thin-film photovoltaic cells. *ACS Appl Mater Interfaces* **3**, 2080–2084 (2011).
- Lan H B, Ding Y C. Nanoimprint lithography. In Wang M. *Lithography* 457–494 (IntechOpen, 2010).
- Wu H, Yang J L, Cao S L, Huang L L, Chen L H. Ordered organic nanostructures fabricated from anodic alumina oxide templates for organic bulk-heterojunction photovoltaics. *Macromol Chem Phys* **215**, 584–596 (2014).
- Choi W M, Park O O. A soft-imprint technique for submicron-scale patterns using a PDMS mold. *Microelectron Eng* **73–74**, 178–183 (2004).
- Lee J H, Kim D W, Jang H, Choi J K, Geng J X *et al.* Enhanced solar-cell efficiency in bulk-heterojunction polymer systems obtained by nanoimprinting with commercially available AAO membrane filters. *Small* **5**, 2139–2143 (2009).
- Aryal M, Buyukserin F, Mielczarek K, Zhao X M, Gao J M *et al.* Imprinted large-scale high density polymer nanopillars for organic solar cells. *J Vac Sci Technol B* **26**, 2562–2566 (2008).
- Hu J C, Shirai Y, Han L Y, Wakayama Y. Template method for fabricating interdigitate p-n heterojunction for organic solar cell. *Nanoscale Res Lett* **7**, 469 (2012).
- Smith A J, Wang C, Guo D N, Sun C, Huang J X. Repurposing Blu-ray movie discs as quasi-random nanoimprinting templates for photon management. *Nat Commun* **5**, 5517 (2014).
- Nootchanat S, Pangdam A, Ishikawa R, Wongravee K, Shinbo K *et al.* Grating-coupled surface Plasmon resonance enhanced organic photovoltaic devices induced by Blu-ray disc recordable and Blu-ray disc grating structures. *Nanoscale* **9**, 4963–4971 (2017).
- Tvingstedt K, Persson N K, Inganäs O, Rahachou A, Zozoulenko I V. Surface Plasmon increase absorption in polymer photovoltaic cells. *Appl Phys Lett* **91**, 113514 (2007).
- Lu F F, Zhang W D, Huang L G, Liang S H, Mao D *et al.* Mode evolution and nanofocusing of grating-coupled surface Plasmon polaritons on metallic tip. *Opto-Electron Adv* **1**, 180010 (2018).
- Liu C H, Hong M H, Cheung H W, Zhang F, Huang Z Q *et al.* Bimetallic structure fabricated by laser interference lithography for tuning surface Plasmon resonance. *Opt Express* **16**, 10701–10709 (2008).
- Chomkitichai W, Ninsonti H, Baba A, Phanichphant S, Shinbo K *et al.* Multiple plasmonic effect on photocurrent generation of metal-loaded titanium dioxide composite/dye films on gold grating surface. *Surf Interface Anal* **46**, 607–612 (2014).
- Hara K, Lertvachirapaiboon C, Ishikawa R, Ohdaira Y, Shinbo K *et al.* Inverted organic solar cells enhanced by grating-coupled surface plasmons and waveguide modes. *Phys*

- Chem Chem Phys* **19**, 2791–2796 (2017).
30. Phetsang S, Phengdaam A, Lertvachirapaiboon C, Ishikawa R, Shinbo K *et al.* Investigation of a gold quantum dot/plasmonic gold nanoparticle system for improvement of organic solar cells. *Nanoscale Adv* **1**, 792–798 (2019).
 31. Pangdam A, Nootchanat S, Lertvachirapaiboon C, Ishikawa R, Shinbo K *et al.* Investigation of gold quantum dot enhanced organic thin film solar cells. *Part Part Syst Charact* **34**, 1700133 (2017).
 32. Pangdam A, Nootchanat S, Ishikawa R, Shinbo K, Kato K *et al.* Effect of urchin-like gold nanoparticles in organic thin-film solar cells. *Phys Chem Chem Phys* **18**, 18500–18506 (2016).
 33. Wang D H, Kim D Y, Choi K W, Seo J H, Im S H *et al.* Enhancement of donor-acceptor polymer bulk heterojunction solar cell power conversion efficiencies by addition of Au nanoparticles. *Angew Chem Int Ed* **50**, 5519–5523 (2011).
 34. Wu J L, Chen F C, Hsiao Y S, Chien F C, Chen P L *et al.* Surface plasmonic effects of metallic nanoparticles on the performance of polymer bulk heterojunction solar cells. *ACS Nano* **5**, 959–967 (2011).
 35. Yang J, You J B, Chen C C, Hsu W C, Tan H R *et al.* Plasmonic polymer tandem solar cell. *ACS Nano* **5**, 6210–6217 (2011).
 36. Li X H, Choy W C H, Huo L J, Xie F X, Sha W E I *et al.* Dual plasmonic nanostructures for high performance inverted organic solar cells. *Adv Mater* **24**, 3046–3052 (2012).
 37. Millstone J E, Hurst S J, Métraux G S, Cutler J I, Mirkin C A. Colloidal gold and silver triangular nanoprisms. *Small* **5**, 646–664 (2009).
 38. Notarianni M, Vernon K, Chou A, Aljada M, Liu J Z *et al.* Plasmonic effect of gold nanoparticles in organic solar cells. *Solar Energy* **106**, 23–37 (2014).
 39. Singh A, Dey A, Das D, Iyer P K. Combined influence of plasmonic metal nanoparticles and dual cathode buffer layers for highly efficient rrP3HT: PCBM-based bulk heterojunction solar cells. *J Mater Chem C* **5**, 6578–6587 (2017).
 40. Otieno F, Shumbula N P, Airo M, Mbuso M, Moloto N *et al.* Improved efficiency of organic solar cells using Au NPs incorporated into PEDOT: PSS buffer layer. *AIP Adv* **7**, 085302 (2017).
 41. Baek S W, Noh J, Lee C H, Kim B S, Seo M K *et al.* Plasmonic forward scattering effect in organic solar cells: a powerful optical engineering method. *Sci Rep* **3**, 1726 (2013).
 42. Pastoriza-Santos I, Liz-Marzán L M. Colloidal silver nanoplates. State of the art and future challenges. *J Mater Chem* **18**, 1724–1737 (2008).
 43. Parnklang T, Lertvachirapaiboon C, Pienpinijtham P, Wongravee K, Thammacharoen C *et al.* H₂O₂-triggered shape transformation of silver nanospheres to nanoprisms with controllable longitudinal LSPR wavelengths. *RSC Adv* **3**, 12886–12894 (2013).
 44. Wongravee K, Parnklang T, Pienpinijtham P, Lertvachirapaiboon C, Ozaki Y *et al.* Chemometric analysis of spectroscopic data on shape evolution of silver nanoparticles induced by hydrogen peroxide. *Phys Chem Chem Phys* **15**, 4183–4189 (2013).
 45. Kozanoglu D, Apaydin D H, Cirpan A, Esenturk E N. Power conversion efficiency enhancement of organic solar cells by addition of gold nanostars, nanorods, and nanospheres. *Org Electron* **14**, 1720–1727 (2013).
 46. Li X H, Ren X G, Xie F X, Zhang Y X, Xu T T *et al.* High-performance organic solar cells with broadband absorption enhancement and reliable reproducibility enabled by collective plasmonic effects. *Adv Opt Mater* **3**, 1220–1231 (2015).
 47. Catchpole K R, Polman A. Plasmonic solar cells. *Opt Express* **16**, 21793–21800 (2008).
 48. Catchpole K R, Polman A. Design principles for particle Plasmon enhanced solar cells. *Appl Phys Lett* **93**, 191113 (2008).
 49. Gu M, Ouyang Z, Jia B H, Stokes N, Chen X *et al.* Nanoplasmonics: a frontier of photovoltaic solar cells. *Nanophotonics* **1**, 235–248 (2012).
 50. Chen X, Jia B H, Saha J K, Cai B Y, Stokes N *et al.* Broadband enhancement in thin-film amorphous silicon solar cells enabled by nucleated silver nanoparticles. *Nano Lett* **12**, 2187–2192 (2012).
 51. Yang Y G, Feng S L, Li M, Wu Z W, Fang X *et al.* Structure, optical absorption, and performance of organic solar cells improved by gold nanoparticles in buffer layers. *ACS Appl Mater Interfaces* **7**, 24430–24437 (2015).
 52. Nootchanat S, Phengdaam A, Ishikawa R, Lertvachirapaiboon C, Shinbo K *et al.* Plasmonic-enhanced photocurrent generation of organic photovoltaics induced by 1D grating and 2D crossed grating structures. *J Nanosci Nanotechnol* **19**, 4727–4731 (2019).
 53. Lertvachirapaiboon C, Maruyama T, Baba A, Ekgasit S, Shinbo K *et al.* Optical sensing platform for the colorimetric determination of silver nanoprisms and its application for hydrogen peroxide and glucose detections using a mobile device camera. *Anal Sci* **35**, 271–276 (2019).
 54. Fu Q, Sun W B. Mie theory for light scattering by a spherical particle in an absorbing medium. *Appl Opt* **40**, 1354–1361 (2001).
 55. Mattis R L, Baroody Jr A J. Carrier lifetime measurement by the photoconductive decay method. *NBS Technical Note* **736**, 1–52 (1972).

Acknowledgements

This research was supported by the Japan Society for the Promotion of Science (JSPS) KAKENHI Grant Number JP16K13662 and JP17H03231. T. P. and K. O. would like to thank the supports from the Center of Excellence for Innovation in Chemistry (PERCH-CIC), Department of Chemistry, Faculty of Science, and the Graduate School, Chiang Mai University. K. O. wishes to thank Center of Excellence in Materials Science and Technology, Chiang Mai University for support under the administration of Materials Science Research Center, Faculty of Science, Chiang Mai University. This research work was partially supported by Chiang Mai University.

Competing interests

The authors declare no competing financial interests.

Supplementary information

Supplementary information for this paper is available at <https://doi.org/10.29026/oea.2019.190010>